Omnidirectional Optical Engineering and Ternary Strategy for High-Performance Indoor Organic Photovoltaics

Kaiwen Zheng, Baozhong Deng, Zhouyi Lu, Luqiao Yin, Shenghao Wang, Hongliang Dong, Esther Mbina, Kekeli N'Konou, Bruno Grandidier, Tao Xu

To cite this version:

Kaiwen Zheng, Baozhong Deng, Zhouyi Lu, Luqiao Yin, Shenghao Wang, et al.. Omnidirectional Optical Engineering and Ternary Strategy for High-Performance Indoor Organic Photovoltaics. Solar RRL, 2024, 10.1002/solr.202400483 . hal-04679575

HAL Id: hal-04679575
https://hal.science/hal-04679575v1

Omnidirectional optical engineering and ternary strategy for high-performance indoor organic photovoltaics

Kaiwen Zheng, Baozhong Deng, Zhouyi Lu, Luqiao Yin[*]*, Shenghao Wang, Hongliang Dong, Esther Mbina, Kekeli N'konou, Bruno Grandidier, Tao Xu*[*]

Kaiwen Zheng, Baozhong Deng, Zhouyi Lu
Sino-European School of Technology, Shanghai University, 200444 Shanghai, China

Luqiao Yin
School of Microelectronics, Shanghai University, 200444 Shanghai, China
E-mail: lqyin@shu.edu.cn

Shenghao Wang
Materials Genome Institute, Shanghai University, 200444 Shanghai, China

Hongliang Dong
Center for High Pressure Science and Technology Advanced Research, 201203 Shanghai, China

Esther Mbina, Kekeli N'konou, Bruno Grandidier
Université de Lille, CNRS, Centrale Lille, Université Polytechnique Hauts-de-France, Junia-ISEN, UMR 8520 - IEMN, 59000 Lille, France
Tao Xu
Sino-European School of Technology, Shanghai University, 200444 Shanghai, China
School of Microelectronics, Shanghai University, 200444 Shanghai, China
E-mail: xtld@shu.edu.cn

Abstract

Indoor organic photovoltaics (IOPVs) with tunable absorption spectra and relatively high power conversion efficiency (PCE) have emerged as one of the most promising energy sources for IoT devices, but enhancing the device performance under various directions of indoor illumination is challenging. Herein, we propose to combine omnidirectional optical engineering and ternary strategy for achieving high-performance IOPVs. We take advantage of a ternary bulk heterojunction (BHJ) with a polymer donor having aligned absorption spectra with the LED spectrum and a guest component that not only blue-shifts the near-infrared absorption of the acceptor but also improves electrical and morphological properties of the BHJ. We further develop a 2D photonic-structured anti-reflection coating to selectively improve the light absorption of IOPVs, leading to a PCE of 29.07% under 1000 lux LED illumination. More importantly, the anti-reflection coating maintained the initial PCE even when irradiated by light incident at large angles, demonstrating an omnidirectional effectiveness. This weaker angular dependency on light absorption provides practical prospects for future sustainable indoor photovoltaic systems.

Keywords: indoor organic photovoltaics, ternary strategy, 2D photonic-structured crystals, anti-reflection coating, omnidirectional

1. Introduction

As Internet of Things (IoT) technologies including sensors, distributed processors and smart switches become more prevalent, there is an urgent need for sustainable power sources to meet the increasing energy demand of connected devices.[1-5] Indoor photovoltaic (IPV) systems, which utilize artificial light sources such as light-emitting diodes (LEDs), provide a promising solution. By taking advantage of the ubiquitous presence of LED lighting commonly used in commercial and residential environments, IPVs offer a strategic method to harvest energy directly from the environment in which IoT devices operate, thereby reducing reliance on traditional energy sources and increasing the sustainability of IoT ecosystems.[6-12] In this context, organic photovoltaics (OPVs) have emerged as one of the most promising technologies for indoor applications, primarily due to the tunable absorption spectra of organic photovoltaic materials that can be precisely controlled to align with the emission spectra of LEDs.[13-17] To date, the power conversion efficiency (PCE) over 20% has been demonstrated for OPVs by using various device engineering approaches such as the use of ternary bulk heterojunction (BHJ).[18-20] In addition, the relatively controlled indoor conditions and low-intensity lighting further mitigate the well-known humidity and light instability issues associated with OPVs, leading to extended device lifetime in indoor environment.[21, 22] To improve the performance of indoor organic photovoltaics (IOPVs) under LED lighting, one effective method is to select suitable organic photovoltaic materials that absorb in the wavelength range of the LEDs emission spectrum. For example, Yan et al. synthesized a highly crystalline acceptor, FCC-Cl, with an absorption peak at 680 nm and achieved a PCE of 30.1% under LED at 2000 lux.[23] Lee et al. incorporated a guest acceptor called ITIC-Th into PM6:IT-4F binary BHJ, resulting in an increase in PCE from 22.5 to 27.8% under the indoor illumination.[24]

Apart from the material innovation in IOPVs, optical engineering methods such as plasmonics, Bragg reflectors, light-coupling layers and photonic-structured crystals, represent an alternative approach to enhance the light harvesting in the predesigned wavelength range, thereby boosting the device performance, especially under conditions of weak illumination.[25-30] Among them, photonic crystals are characterized by their simplicity in structure and ease of fabrication, leading to widespread use in photovoltaic cells.[31] Photonic crystals feature a periodic arrangement of dielectric constants that establishes a photonic bandgap, facilitating the control and manipulation of light propagation. For example, nanostructured photonic crystals attached to the backside of the glass substrate can contribute to an increase of 20% in light coupling efficiency of OPVs.[32] Another important optical factor is the angle dependent light absorption, considering that IOPVs mostly receive LEDs light at various angles and the device performance depends strongly on the angle of the incident light.[33] Therefore, meticulous design of the photonic crystals is needed for achieving omnidirectional absorption enhancement.

In this work, we combine omnidirectional optical engineering and ternary strategy to improve the indoor light absorption for achieving high-performance IOPVs. First, a ternary BHJ with a polymer donor having aligned absorption spectra with the LED spectrum and a guest component that not only blue-shifts the near-infrared absorption of the acceptor but also improves electrical and morphological properties of the BHJ, was used in IOPVs. Subsequently, a 2D photonic-structured anti-reflection (AR) coating was applied to the rear side of the device to selectively reduce the reflection loss, leading to a PCE of 29.07% under 1000 lux LED illumination for optimal IOPV. The dependence of the device performances on the incident angle of the light was further assessed. The AR coating was found to be beneficial to maintain a high PCE when the device was irradiated by light incident at large angles. Such a result highlights the effectiveness of omnidirectional optical engineering in ensuring consistent performance of IOPVs under the oblique incidence of light, which is beneficial for indoor applications.

2. Result and discussion

Figure 1a shows the schematic configuration of IOPVs comprising stacked ITO/poly(3,4-ethylenedioxythiophene):poly (styrene sulfonate) (PEDOT:PSS)/BHJ/ PNDIT-F3N/Ag layers. A 40 nm-thick PEDOT: PSS and 10 nm-thick PNDIT-F3N were used as hole transport layer and electron transport layer, respectively, to ensure the charge collection in IOPVs. A 120 nm-thick Ag was used as the top electrode. The thickness of the

BHJ layer was kept at 140 nm. For the binary device configuration, the BHJ active layer was composed of a donor PM6 and an acceptor BTP-eC9. A guest acceptor L8-BO was incorporated into the active layer, thus forming a ternary device configuration. The chemical structures of these materials are depicted in **Figure 1**b. The schematic energy-level diagram of the functional materials used in IOPV is shown in **Figure 1**c, the improved alignment of the highest occupied molecular orbital (HOMO) and the lowest unoccupied molecular orbital (LUMO) in the ternary device facilitates efficient charge transport and extraction and suppresses energy loss. **Figure 1**d presents the normalized absorption spectra of both the binary and ternary blends. The donor PM6 exhibits strong absorption in the visible wavelength that matches well with the emission spectra of the LEDs. The absorption peak of L8-BO is blue-shifted from 830 nm to 790 nm compared to BTP-eC9, as shown in **Figure S1** (Supporting Information), resulting in a slight shift of the absorption edge from the near-infrared region into the visible region.

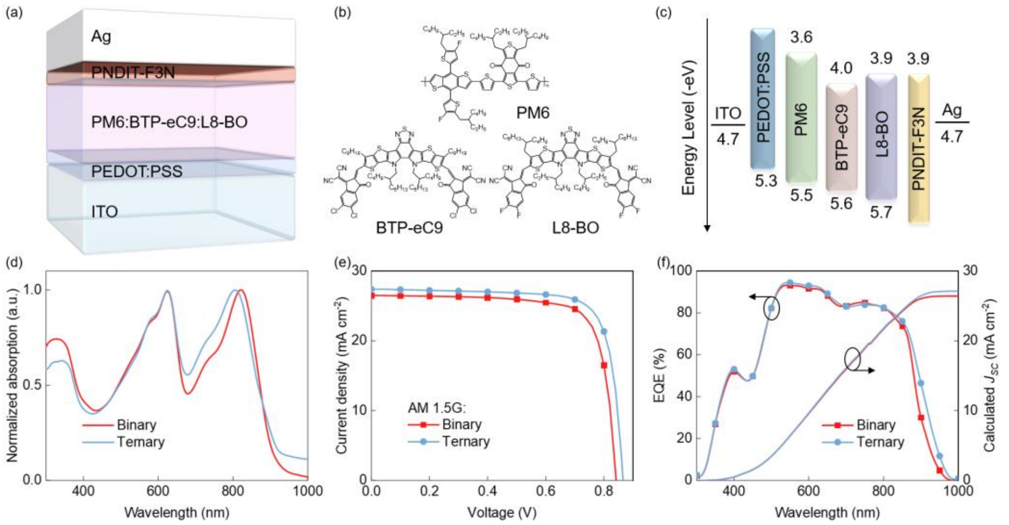

Figure 1. a) Device structure of IOPVs. b) Chemical structures of polymer donor PM6 and two acceptors including BTP-eC9 and L8-BO. c) Schematic energy-level diagram of the functional materials used in IOPVs. d) Normalized absorption spectra of the binary and ternary BHJ films. e) *J*-*V* characteristic, and f) EQE spectra with the calculated J_{SC} measured for the binary and ternary devices.

Next, a set of IOPVs was fabricated based on the binary BHJ of PM6:BTP-eC9 and the ternary BHJ of PM6:BTP-eC9:L8-BO to investigate the influence of ternary strategy on the device performance. The current density-voltage (*J*-*V*) characteristics under AM1.5G illumination of the binary and ternary devices are shown in **Figure 1**e. A summary of the open circuit voltage (V_{OC}), short circuit current density (J_{SC}), fill factor (FF) and PCE is listed in **Table 1**. The performance of the binary device, which yielded a PCE of 17.42% with a V_{OC} of 0.85 V, a J_{SC} of 26.49 mA cm^{-2}, and a FF of 77.86%, is consistent with our previous report.[31] For the ternary device, a PCE of 18.64% was obtained with a V_{OC} of 0.87 V, a J_{SC} of 27.36 mA cm^{-2} and a FF of 78.65%, which is evidently higher than those of the binary device. The integrated current density (calculated J_{SC}), derived from the external quantum efficiency (EQE) spectra presented in **Figure 1**f, is consistent with the experimental results, which confirms the reliability of our data. The EQE spectra between 500 – 650 nm and the photocurrent generation are slightly enhanced by applying the ternary strategy, which is beneficial for improving device performance under indoor illumination.

Table 1. Summary of photovoltaic parameters measured for the binary and ternary device under AM 1.5G. The results were averaged from the measurements of ten devices.

Illumination	Device	V_{OC} (V)	J_{SC} (mA cm^{-2})	Calculated J_{SC} (mA cm^{-2})	FF (%)	PCE (%)
AM 1.5G	Binary	0.85±0.01	26.49±0.23	26.39	77.86±0.25	17.42±0.12
	Ternary	0.87±0.01	27.36±0.15	27.11	78.65±0.05	18.64±0.04

To simulate the indoor illumination, we employed the commonly used 3000K LED as light source. As shown in **Figure 2**a, the emission power spectra of 3000K LED at 1000, 1500 and 2000 lux are measured with a spectrometer providing an integral power intensity (P_{in}) of 366, 578 and 817 µW cm^{-2}, respectively. **Figure 2**b and **Table 2** show the *J*-*V* characteristics and the corresponding photovoltaic parameters of the binary and ternary devices under LED illumination. The PCE value under indoor illumination is calculated using the following equation:

$$\text{PCE} = \frac{V_{OC} \times J_{SC} \times FF}{P_{in}} \#(1)$$

At 1000 lux, the binary device yielded a PCE of 25.10%, with a V_{OC} of 725.75 mV, a J_{SC} of 161.28 µA cm^{-2} and a FF of 78.48%. In contrast, the ternary device exhibited a superior PCE of 26.93%, with a V_{OC} of 748.87 mV, a J_{SC} of 166.17 µA cm^{-2} and a FF of 79.21%. Furthermore, the photovoltaic performance was evaluated under illumination intensities of 1500 and 2000 lux to cover the entire spectrum of indoor lighting, giving evidence of similar enhancement. Under LED illumination, the ternary device exhibits a higher J_{SC}, which is consistent with the favorable absorption spectrum and the enhanced calculated J_{SC} presented in **Figures 2**d-f. Additionally, the long-term indoor light cycling (10 h dark/14 h light) stability was assessed for the ternary device to simulate real-world operational environment. The device was encapsulated and stored in a N_2-filled glovebox. As shown in **Figure 2**c, the ternary device remains 84% of its initial PCE after 1500 h. The good stability observed can be attributed to stable carrier dynamics within the device.

Table 2. Summary of photovoltaic parameters measured for the binary and ternary device under 3000K LED at 1000 lux, 1500 lux, and 2000 lux. The results were averaged from the measurements of ten devices.

Illumination	P_{in} (µW cm^{-2})	Device	V_{OC} (mV)	J_{SC} (µA cm^{-2})	Calculated J_{SC} (µA cm^{-2})	FF (%)	PCE (%)
LED 1000 lux	366	Binary	725.75	161.28±0.30	156.92	78.48±0.06	25.10±0.04
		Ternary	748.87	166.17±0.16	158.57	79.21±0.47	26.93±0.21
LED 1500 lux	578	Binary	734.89	250.40±0.72	243.72	78.93±0.22	25.13±0.32
		Ternary	756.60	253.81±0.22	246.27	79.93±0.43	26.56±0.19
LED 2000 lux	817	Binary	745.73	348.19±0.36	342.20	79.18±0.19	25.16±0.14
		Ternary	766.32	353.23±0.24	345.79	80.49±0.24	26.67±0.16

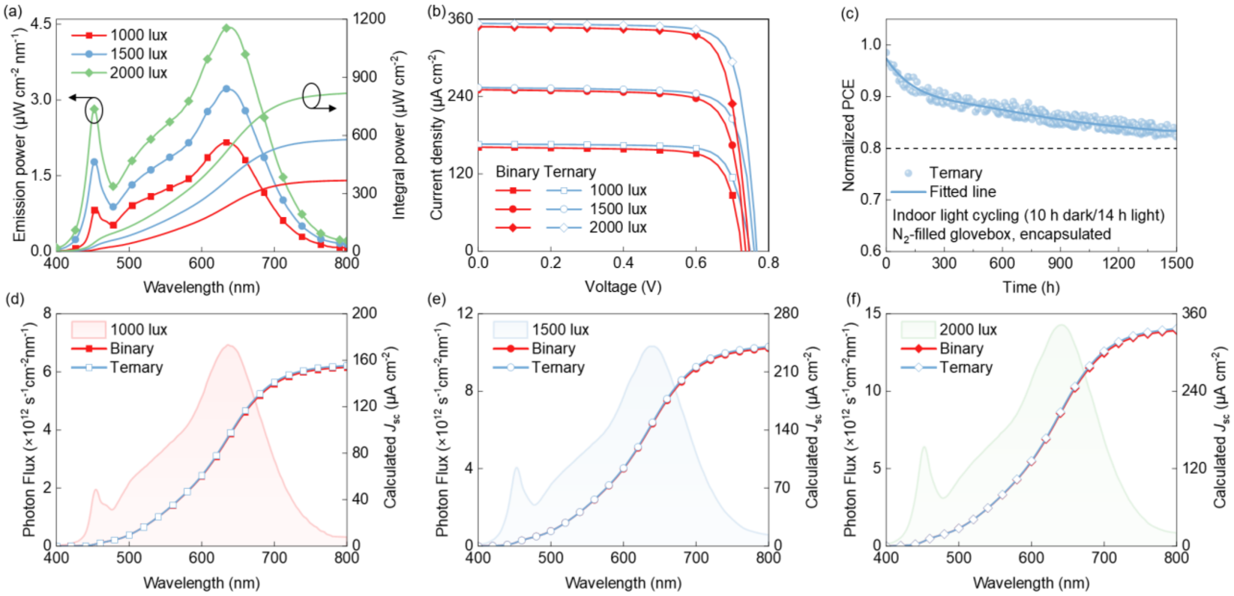

Figure 2. a) The emission power spectrum and the integral input power of 3000K LED at 1000 lux, 1500 lux, and 2000 lux. b) *J-V* characteristics of the binary and ternary device under 3000K LED at 1000 lux, 1500 lux, and 2000 lux. c) The long-term indoor light cycling (10 h dark/14 h light) stability curve of the ternary device. The photon flux curves of d) 1000 lux, e) 1500 lux, and f) 2000 lux and the corresponding calculated J_{SC} of the binary and ternary device.

The carrier dynamics properties were systematically investigated to get a deep insight on the effect of the ternary strategy in IOPV. **Figure 3**a shows the dark *J-V* curves of both binary and ternary devices. Notably, the ternary device exhibits a reduced saturated dark current density, which suggests a decrease in leakage current and a reduction in energy loss. This observation is consistent with the lower fitted transfer resistance derived from the Nyquist plots in the electrochemical impedance spectroscopy (EIS) characterization,[34, 35] as shown in **Figure 3**b. Next, photocurrent density (J_{ph})-effective voltage (V_{eff}) characteristics of both devices were measured and plotted in **Figure 3**c, where $J_{ph} = J_1 - J_d$, J_1 is the current density measured under the illumination under AM 1.5G and J_d is the dark current density. V_{eff} is determined as $V_{eff} = V_0 - V_{app}$, where V_0 is the built-in potential and V_{app} is the applied bias. V_0 is obtained by the voltage where J_{ph} is 0. The ternary device enables a higher J_{ph}. As the J_{ph} of both devices saturates nearly at the same V_{eff}, a more efficient exciton dissociation probability (P_{diss}) can be observed in ternary device. P_{diss} is determined as $P_{diss} = \frac{Jsc}{Jsat}$, where J_{sat} is saturated current and can be obtained by the J_{ph} where V_{eff} is 2 V.[36] P_{diss} is then calculated and plotted in **Figure S2**a (Supporting Information). The P_{diss} is 98.64% for the ternary device, which is higher than that of the binary device (95.81%). The charge collection probability (P_{CC}) is determined as $P_{\mathrm{CC}} = \frac{J_{power}}{J_{sat}}$, where J_{power} is the work current and can be obtained by the current density where output power is maximum. As shown in **Figure S2**b (Supporting Information), the value of P_{CC} is found to increase from 87.22% to 89.70% for the ternary device, comparing with that of the binary device. Therefore, the enhancement of P_{diss} and P_{CC} indicates that the ternary device has a more effective capacity for exciton dissociation and charge collection. In addition, the relationship between V_{OC} and J_{SC} concerning LED light intensity (P) is depicted in **Figure 3**d. According to the equation $V_{\mathrm{OC}} \propto n(kT/q)\ln P$, we observed the slope of the ternary device is 1.057 kT/q (where K, T and q are the Boltzmann constant, absolute temperature and elementary charge, respectively), slightly lower than that measured for the binary device (1.102 kT/q), indicating an effective suppression of defect-assisted recombination. This suppression is further supported by the increased exponential factor α, extracted from the equation $J_{\mathrm{SC}} \propto P^{\alpha}$, which increases from 0.985 for the binary device to 0.992 for the ternary device, suggesting a reduction in biomolecular recombination. These results demonstrate that the ternary strategy, by incorporating L8-BO, can help enhancing the charge extraction through mitigation of the charge recombination, which leads to a higher J_{SC} and V_{OC}, accounting for the higher device efficiency of IOPV.[37-39] The carrier mobility was measured by using space-charge-limited current (SCLC) method, as shown in **Figure 3**e. Hole-only devices and electron-only devices of both devices were fabricated to calculate the hole mobility (μ_{h}) and electron mobility (μ_{e}) using the SCLC expression described by the Mott-Gurney law:

$$J = \frac{9}{8}\varepsilon_0\varepsilon_r\mu\frac{V^2}{d^3}\#(2)$$

where ε_0, ε_r, μ, and d are the vacuum permittivity (8.85×10^{-12} F m^{-1}), the relative dielectric constant of the active layer (≈3), the carrier mobility and the thickness of the active layer (140 nm), respectively. The structure of hole-only device is ITO/PEDOT: PSS (40 nm)/PM6: BTP-eC9 or PM6: BTP-eC9: L8-BO (140 nm)/MoO_3 (10 nm)/Ag (120 nm). The structure of electron-only device is ITO/ZnO (50 nm)/PM6: BTP-eC9 or PM6: BTP-eC9: L8-BO (140 nm)/PNDIT-F3N (10 nm)/Ag (120 nm). The ternary device shows a slightly higher μ_{h} of

2.835×10^{-4} cm^2 V^{-1} S^{-1} and μ_e of 2.390×10^{-4} cm^2 V^{-1} S^{-1} than that of the binary device (μ_h of 2.780×10^{-4} cm^2 V^{-1} S^{-1} and μ_e of 2.277×10^{-4} cm^2 V^{-1} S^{-1}). A more balanced μ_h/μ_e value of 1.186 is also obtained for the ternary device compared with that of the binary device (1.221), which suggests higher carrier mobility and better percolation pathways for the carriers' transport, leading to a minimized space-charge region and suppressed bimolecular recombination.[40] Furthermore, the trap density (N_t) in the BHJ active layer was investigated *via* SCLC measurements of the electron-only devices, and by the equation of $V_{\mathrm{TFL}} = \frac{qN_t d^2}{2\varepsilon_0\varepsilon_r}$, where V_{TFL} is the trap-filled limit voltage. As shown in **Figure 3**f, the ternary device exhibits a lower V_{TFL}, suggesting a lower N_t of 1.259×10^{15} cm^{-3} as compared with that of the binary device (2.171×10^{15} cm^{-3}). This reduction implies a suppression of nonradiative recombination loss, which agrees with the lower leakage current.

Figure S3a (Supporting Information) shows the photo fluorescence (PL) spectrum of ITO/PEDOT: PSS/BHJ films. The binary film exhibits a PL peak at 920 nm, whereas the ternary film shows a peak blue-shifted to 895 nm. Additionally, pronounced quenching is observed in the ternary film, indicating enhanced hole extraction from the active layer to the HTL.[41] The dynamics of the charge carriers in both devices were also analyzed using the time-resolved photo fluorescence (TRPL) measurements, as shown in **Figure S3**b (Supporting Information). The average exciton lifetime was calculated using triple exponential function fitting method. Ternary device has a shorter exciton lifetime of 25.91 ps, compared to that of the binary device (29.89 ps). The PL and TRPL results demonstrate that the ternary strategy could promote the exciton dissociation inside BHJ while decreasing the radiative recombination at the interfaces between HTL and the active layer. All the carrier dynamics properties are summarized in **Table S1** (Supporting Information), demonstrating that the ternary strategy contributes to improving the electrical properties of IOPVs.

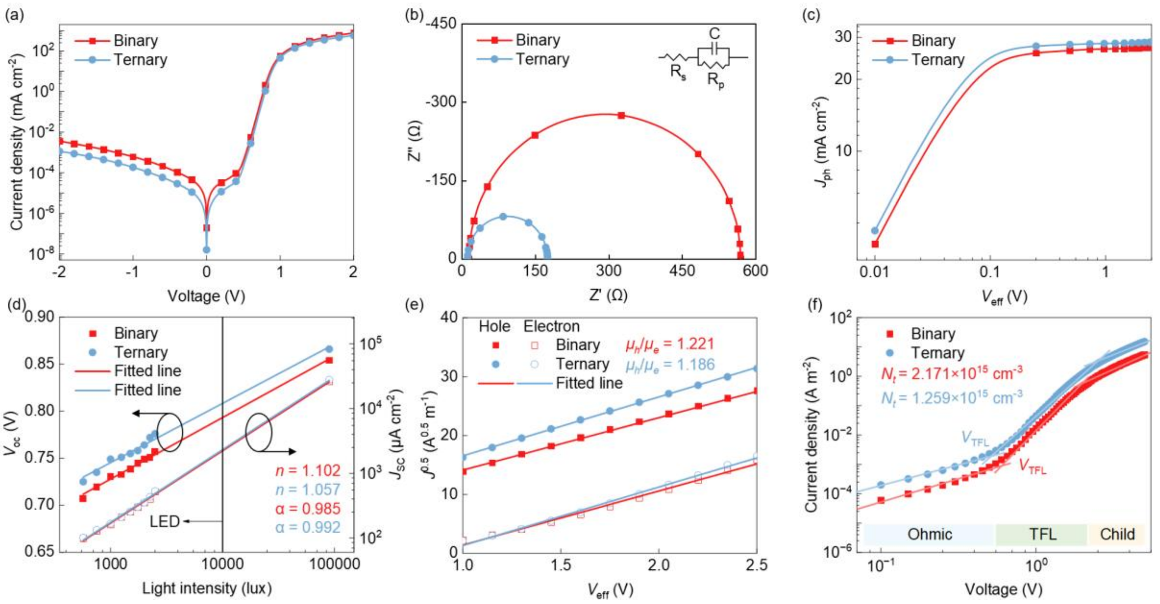

Figure 3. a) The dark *J*-*V* characteristics, b) Nyquist plot under dark illumination at open-circuit conditions, c) J_{ph}-V_{eff}, d) J_{SC}-P and V_{OC}-P characteristics, e) SCLC measurements and f) trap density measurements of the binary and ternary devices in a bias range extending over the Ohmic, Trap-filled-Limit (TFL) and Child regions.

The surface morphology of both binary and ternary BHJ films was analyzed by using atomic force microscopy (AFM), as shown in **Figure 4**a and b. The surface root-mean-square roughness (RMS) is found to decrease from 2.16 to 1.02 nm due to the addition of L8-BO, which suppresses the over aggregation of BTP-eC9 molecules during the formation of the BHJ film. More interestingly, a distinct fiber-like feature can be observed in the ternary BHJ film, suggesting the presence of a fibrillar network that provides pathways for efficient exciton dissociation and charge transport. The high-resolution transmission electron microscope (HR-TEM) measurements were also performed on both BHJ films to get a deep understanding on the morphological evolution, as shown in **Figure S4**a and b (Supporting Information). Similar surface morphology is observed in both BHJ films, indicating that the surface morphology is not degraded by the incorporation of the third component.

Molecular orientation and crystalline properties of both BHJ films were subsequently investigated by grazing incidence wide-angle X-ray scattering (GIWAXS). **Figure 4**c and d shows the 2D scattering patterns of binary and ternary BHJ film, respectively. Both films exhibit prominently face-on orientation. **Figure 4**e shows the 1D profiles along the in-plane

(IP) and out-of-plane (OOP) direction measured for both BHJ films, while the crystallinity properties of two BHJ films are summarized in **Table S2** (Supporting Information). The π–π stacking d-spacing is calculated using the Bragg equation:

$$d = \frac{2\pi}{q} \#(3)$$

where q is the GIWAXS scattering vector of (010) peak. The d-spacing in the OOP direction of the ternary film is 3.670 Å, which is slightly lower than that of the binary BHJ film (3.681 Å). In addition, the lamellar crystal coherence length (CCL) is calculated using the Debye-Scherrer equation:

$$\mathrm{CCL} = 0.9 \times \frac{2\pi}{\mathrm{FWHM}} \#(4)$$

where FWHM is the full width at half maxima of the GIWAXS scattering peak. The CCL in the in-plane direction for ternary film (32.31 Å) is longer than that of the binary BHJ film (31.95 Å), indicating that the molecular packing and crystallinity of the BHJ active layer are slightly improved by the incorporation of L8-BO.

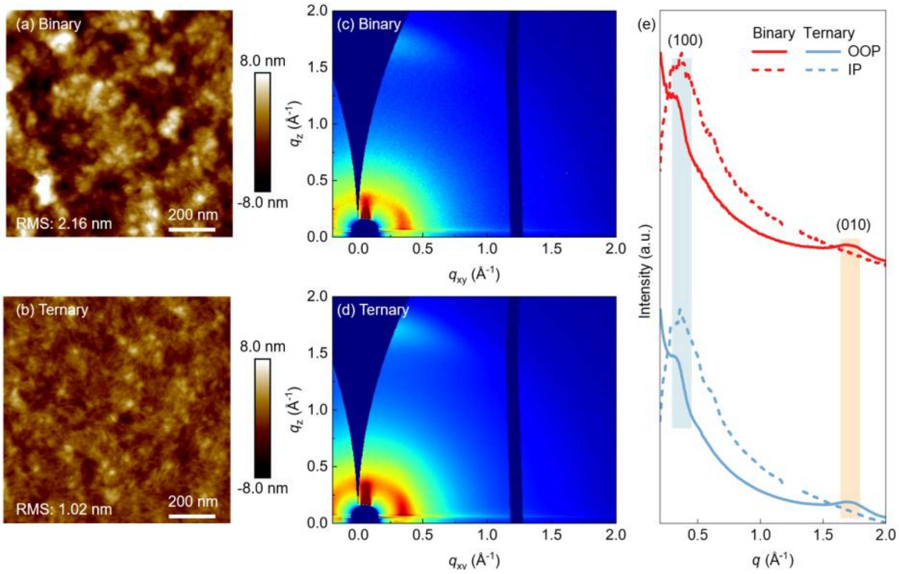

Figure 4. AFM images measured for a) the binary BHJ film, and b) the ternary BHJ film. GIWAXS 2D scattering patterns for c) the binary BHJ film, and d) the ternary BHJ film. e) GIWAXS 1D profiles along the IP and OOP direction measured for both BHJ films.

In addition to improving the electrical performance of IOPVs, it is equally important to minimize the optical loss, in particular to reduce the reflection loss of incident light. Therefore, an optical engineering method was applied to further boost the performance of IOPVs. As shown in **Figure 5**a, to mitigate the reflection at the air/glass interface, a 2D photonic-structured AR coating was fabricated by using nanosphere lithography and nanoimprint techniques as reported in our previous work.[42] The periodicity of the nanopillars in the Si module is around 850 nm and the height of nanopillars is around 600 nm, optimized by the finite element method (FEM) simulation, for realizing the minimal ambient reflection by the IOPVs. The optical constants of all the functional materials used in IOPVs are plotted in **Figure S5** (Supporting Information). **Figure 5**b shows the scanning electron microscope (SEM) image of the nanostructured Si module. An inverted polydimethylsiloxane (PDMS) photonic-structured AR coating formed on the Si module was then carefully peeled-off and attached on the glass side of the IOPVs. The reflection spectra of the glass with and without AR coating is shown in **Figure S6** (Supporting Information), indicating that the AR coating helps to minimize the ambient reflection.

To validate the effectiveness of the 2D photonic-structured AR coating in reducing reflection under LED, the distributions of the electric field ($|E|$) for the ternary device with and without AR coating were calculated at a wavelength of 635 nm (according to the emission power spectrum of 3000K LED as shown **in Figure 2**a). As shown in **Figure 5**c and d, the $|E|$ distribution at 635 nm of the device with the AR coating is remarkably enhanced in ITO and active layer, indicating that more photons are entering the ITO and reinforcing absorption in the active layer. The transmission spectra of the glass with and without the AR coating also agrees with the simulation results, which is beneficial for the absorption of incident indoor light for IOPVs, as shown in **Figure 5**e. **Figure S7** (Supporting Information) presents the normalized absorption spectra of the ternary blends without and with AR coating, confirming the effectiveness of the AR coating. The indoor photovoltaic performance of ternary device with AR coating was then measured, while the corresponding *J-V* characteristics and photovoltaic parameters are summarized in **Figure 5**f. The performance of the device is evidently improved, resulting in a PCE approaching 30% (29.07%) under 1000 lux LED illumination. The calculated J_{SC}, derived from the EQE spectra presented in **Figure S8** (Supporting Information), is consistent with the experimental results. Finally, the stability test for the IOPVs with and without AR coating was performed, as shown in **Figure S9** (Supporting Information). The IOPV with AR coating exhibits a slightly improved stability due to the hydrophobic nature of the PDMS that can limit the permeation of moisture. [43,44]

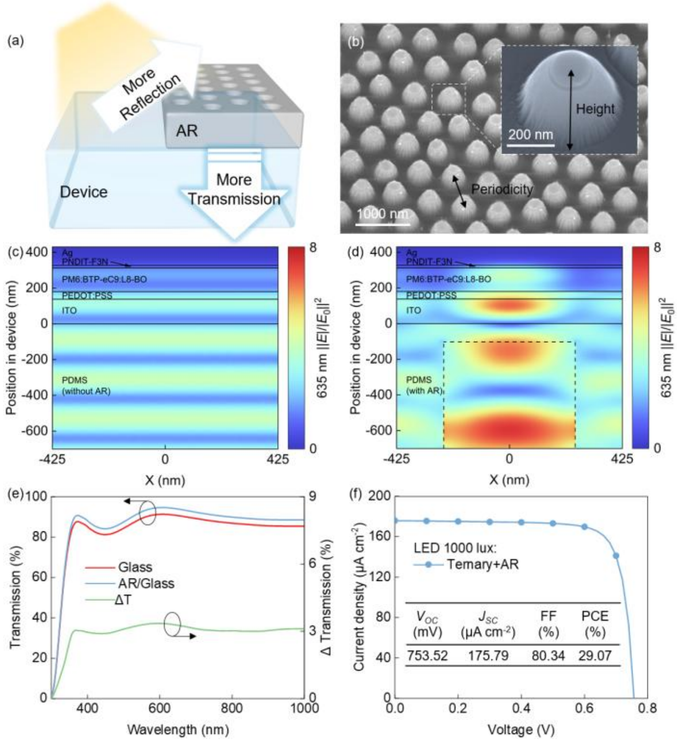

V_{OC} (mV)	J_{SC} (μA cm^{-2})	FF (%)	PCE (%)
753.52	175.79	80.34	29.07

Figure 5. a) Schematic diagram illustrating the optical engineering with the 2D photonic-structured AR coating. b) SEM image of the nanostructured Si module. Distributions of the electric field (|*E*|) calculated at wavelength of 635 nm for c) the device without AR coating and d) the device with the 2D photonic-structured AR coating having a periodicity of 850 nm and a height of 600 nm (dash line area). e) Transmission spectra of the glass with and without the AR coating and the corresponding difference of transmission (ΔTransmission). f) The *J*-*V* characteristics and photovoltaic parameters of the IOPV with the 2D photonic-structured AR coating under 3000K LED at 1000 lux.

It should be noted that the reported PCE of the photovoltaic devices is typically measured under normal incident light conditions. However, in actual indoor applications, IOPVs mostly receive LEDs light at various angles and the performance depends strongly on the angle of the incident light.[45] Therefore, the angular dependence on light absorption should also be optimized. The FEM simulation was employed to simulate the omnidirectional incident light angle scenario in IPVs application. **Figures 6**a and **6**b show the simulated normalized absorption spectra of the IOPVs without and with AR coating under conditions of normal and oblique light incidence, respectively. The device without the AR coating suffered an obvious fast reduction in the absorption. Conversely, a slower decrease in the light absorption was observed for the device with AR coating as the angle of the incident light increases. This different behavior indicates that the AR coating helps reduce the angular dependence of IOPVs with enhanced absorption for the incident light from various directions.

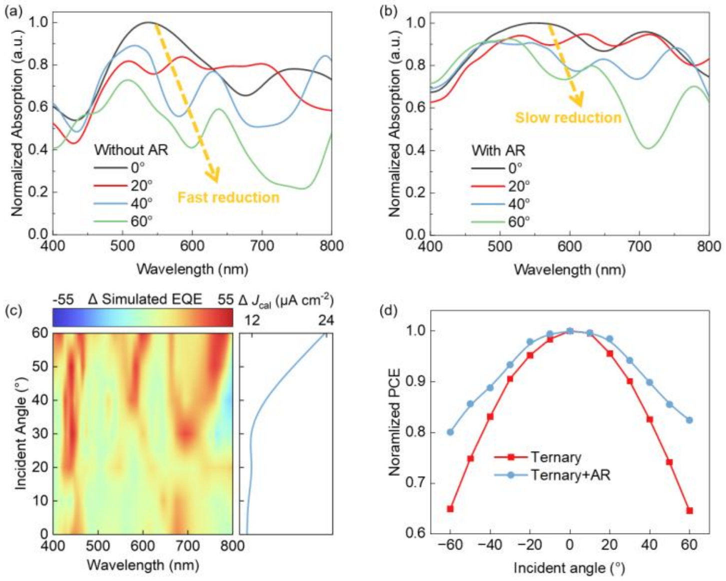

Figure 6. Wavelength-dependent normalized absorption spectra calculated for the IOPVs a) without and b) with the 2D photonic-structured AR coating, at different angles of the incident light. c) The contour map of simulated EQE difference between the IOPVs with and without AR coating as functions of the incident angle and the wavelength, and the line chart of the calculated J_{SC} difference between the IOPVs with and without AR coating under 3000K LED at 1000 lux as a function of the incident angle. d) The normalized PCE curves of the experimental values for the ternary device with and without the AR coating.

To further investigate the AR-induced omnidirectional characteristics, the EQE simulation for the device without and with the AR coating was performed, as shown in **Figure S10**a and S10b (Supporting Information), respectively. **Figure 6**c shows the contour map of simulated EQE difference between the IOPVs with and without AR coating as functions of the incident angle and the wavelength. Based on the contour map, the simulated ΔEQE is superior to zero in the majority of the mapping, which becomes more evident as the incident angle increases. This not only indicates that the AR coating is beneficial for enhancing the light absorption of the devices but also shows that it helps maintain the EQE value at larger incident angles. To clearly demonstrate the omnidirectional enhancement, the difference in calculated J_{SC} values at various incident angles was analyzed, as shown by the line chart of **Figure 6**c. When the incident light is perpendicular to the glass (incident angle = 0°), the calculated J_{SC} difference is 11.20 μA.cm^{-2}, consistent with previous measurements. When the incident angle increases, the calculated J_{SC} difference is increased to 23.75 μA.cm^{-2}. A set of *J-V* tests at different incident angles was then performed. The normalized PCE as a function of incident angle is plotted in **Figure 6**d. When the angle of incident light increases to 60 degrees, IOPV with AR coating can maintain 80% of the original performance at normal incidence, which is significantly higher than that of device without AR (60 %), confirming the AR-induced omnidirectional enhancement for Indoor applications.

3. Conclusion

In conclusion, we propose a device based on a ternary strategy coupled with an omnidirectional optical coating to improve the indoor light absorption and achieve high-performance IOPVs. The guest acceptor does not only blue-shifts the near-infrared absorption of the acceptor, but also improves the electrical and morphological properties of the BHJ. Similarly, the optimized 2D photonic-structured AR coating has two attributes. It selectively reduces the reflection loss in IOPVs and ensures an efficient harvesting of light at oblique incidences. Both features are essential to reach high PCEs under 1000 lux LED illumination, making this sustainable technology closer to commercialization.

4. Experimental Section

Materials: PDMS and corresponding curing agent were purchased from Shanghai Dejishangmao Ltd. Poly(3,4-ethylenedioxythiophene):poly (styrene sulfonate) (PEDOT:PSS (Clevios PVP AI 4083)) and ZnO solution was purchased from Xi’An Polymer Light Technology Corp. Poly[(2,6-(4,8-bis(5-(2-ethylhexyl-3-fluoro)thiophen-2-yl)-benzo[1,2-b:4,5-b’]dithiophene))-alt-(5,5-(1’,3’-di-2-thienyl-5’,7’-bis(2-ethylhexyl)benzo[1’,2’-c:4’,5’-c’]dithiophene-4,8-dione)] (PM6), 2,2'-((2Z,2'Z)-((12,13-bis(2-ethylhexyl)-3,9-(2-butyloctyl)-12,13-dihydro-[1,2,5]thiadiazolo[3,4-e]thieno[2'',3’':4’,5']thieno[2',3':4,5]pyrrolo[3,2-g]thieno[2',3':

4,5]thieno[3,2-b]indole-2,10-diyl)bis(methanylylidene))bis(5,6-difluoro-3-oxo-2,3-dihydro-1H-indene-2,1-diylidene))dimalononitrile (L8-BO), 2,2'- [[12,13-Bis(2-butyloctyl)-12,13-dihydro-3,9-dinonylbisthieno[2'',3'':4',5']thieno[2',3':4,5]pyrrolo[3,2-e:2',3'-g][2,1,3]benzothiadiazole-2,10-diyl]bis[methylidyne(5,6-chloro-3-oxo-1H-indene-2,1(3H)-diylidene)]]bis[propanedinitrile] (BTP-eC9) and Poly[[2,7-bis(2-ethylhexyl)-1,2,3,6,7,8-hexahydro-1,3,6,8-tetraoxobenzo[lmn][3,8]phenanthroline-4,9-diyl]-2,5-thiophenediyl[9,9-bis[3-(dimethylamino)propyl]-9H-fluorene-2,7-diyl]-2,5-thiophenediyl (PNDIT-F3N) were purchased from Organtec Ltd. 1,8-diiodooctane (DIO) and chloroform (CF) were purchased from Sigma-Aldrich. All materials purchased were used without further purification.

Device Fabrication: The ITO/glass substrates with a sheet resistance of 15 Ω sq^{-1} were cleaned by ultrasonication sequentially with detergent, deionized water, acetone and isopropanol each for 30 min. After cleaning, the ITO/glass substrates were treated with plasma for 5 min. The PEDOT:PSS solution was then deposited on ITO/glass substrates by using spin-coating with 3000 rpm for 30 s, followed by an annealing at 130 ℃ for 20 min, to form a 40 nm-thick HTL. Next, the binary (PM6:BTP-eC9 16mg mL^{-1} , 1:1.2 w/w, dissolved in CF with 0.5 vol% DIO as additive) or ternary (PM6:L8-BO:BTP-eC9 16mg mL-1, 1:0.8:0.4 w/w/w, dissolved in CF with 0.5 vol% DIO as additive) solution, was spin coated on the prepared HTL at 3500 rpm (binary) or 4000 rpm (ternary) for 30 s, followed by an annealing at 100℃ for 10 min in a N_2-filled glove box, thus forming a 140 nm-thick active layer. PNDIT-F3N solution (1 mg mL^{-1} dissolved in methanol with 5 vol% acetic acid as co-solvent) was spin coated on the active layer at 3000 rpm for 30 s, to form a 10 nm-thick ETL. Finally, a 120 nm-thick Ag as upper metal electrode was deposited by thermal evaporation under high vacuum (5×10^{-4} Pa) with an evaporation rate of 2~3 Å s^{-1}. The IOPVs possess an active area of 5 mm^2, defined by the crossover area between ITO and upper Ag electrode.

Characterization: The *J-V* characteristics of the devices were measured by a source meter (Keithley 2420). For the one sun performance, the photocurrent was measured under a calibrated AM 1.5G solar spectrum simulator (Newport Oriel Sol3A) (100 mW cm^{-2}). For the indoor performance, the photocurrent was measured under a 3000K intensity adjustable LEDs (IWATA GP01). The emission power spectrum of this LED at different light intensity was measured by a spectrometer (HP350C, Hangzhou LCE Intelligent Detection Instrument Ltd.). The EQE was measured using a 7-SCSpec solar cell measurement system (7-STAR Co.). The absorption and transmission spectra of the binary and ternary films were measured by using a UV-Vis spectrometer (Jasco V-750). The PL and TRPL were measured by a fluorescence spectrometer (Nano finder 30A, Tokyo Instruments, INC.). Impedance spectroscopy was measured using an impedance analyzer (Corrtest CS2350H) with a bias of 0.8 V over the frequency range from 0.1 Hz to 1 MHz under dark condition. The surface morphologies of different films were analyzed by using AFM (Nanonavi SPA-400SPM). The HR-TEM images were obtained by using a Themis ETEM G3 microscope, the samples were prepared on the ultra-thin carbon films . SEM images were obtained using a ZEISS Sigma 500 microscope. The GIWAXS measurements were performed using an incident angle of 0.15° at the BL14B station of the Shanghai Synchrotron Radiation Facility.

Theoretical simulation: The wavelength-dependent reflection, $R(\lambda)$, absorption, $A(\lambda)$, and the profile of the electric field, $E(x, \lambda)$, in the IOPVs were analyzed using transfer matrix method (TMM) over the wavelength range from 400 to 800 nm. Refractive indices of PDMS, ITO and Ag layers are taken from refractiveindex.info database. The optical constants of the functional layers of the PEDOT: PSS, BHJ, and PNDIT-F3N were measured using a spectroscopic ellipsometer (J.A. Woollam RC2-XI). In the simulation, the incoming light is considered from the glass side and normal (or inclined) to the device, and the functional layers are regarded as the homogenous media with the optical properties determined by the wavelength dependent optical constants. Assuming no non-geminate recombination losses, the theoretical predication of the $A(\lambda)$ and $EQE(\lambda)$ in the IOPVs was calculated using the following expressions:

$$A(\lambda) = \int (2\pi\varepsilon_0 c n(\lambda) k(\lambda))/\lambda \, |E(x,\lambda)|^2 dx$$

$$EQE(\lambda) = A(\lambda) IQE(\lambda)$$

where ε_0 is vacuum permittivity, c is the speed of light, $n(\lambda)$ and $k(\lambda)$ are the wavelength dependent refractive index and extinction coefficient of the perovskite layer, x is position of the electric field in the perovskite layer, IQE = 100%.

The performance of the IOPVs with a 2D photonic structured AR coating was analyzed using the COMSOL Multiphysics. The periodicity of 2D photonic structured AR coating is defined by the dimension of the simulation unit. The AR coatings, with a pitch size of 850 nm and a nanohole depth of 600 nm, were optimized and examined for the performance of the IOPVs with a layer configuration of AR coating /ITO (150 nm)/PEDOT: PSS (40 nm)/ BHJ (140 nm)/ PNDIT-F3N (10 nm)/Ag (120 nm). To improve the calculating efficiency, only one simulation unit including one nanohole was simulated. To enhance the reliability of the simulation, the mesh size was set to 20 nm, which is small enough to ensure the accuracy and big enough to meet the calculating efficiency. All simulations were operated on a server (12th Gen Intel(R) Core(TM) i9-12900 2.40 GHz, 128 GB).

Supporting Information

Supporting Information is available from the Wiley Online Library or from the author.

Acknowledgements

This work was supported by National Natural Science Foundation of China (12174244) and the Open Fund of Key Laboratory of Advanced Display and System Applications of Ministry of Education, Shanghai University, China.

Received: ((will be filled in by the editorial staff))
Revised: ((will be filled in by the editorial staff))
Published online: ((will be filled in by the editorial staff))

References

1. Xie, L.,Song, W.,Ge, J.,Tang, B.,Zhang, X.,Wu, T.,Ge, Z., *Nano Energy* **2021,** *82*, 105770.
2. Mainville, M.,Leclerc, M., *ACS Energy Lett.* **2020,** *5*, 1186-1197.
3. Cui, Y.,Hong, L.,Hou, J., *ACS Appl. Mater. Interfaces* **2020,** *12*, 38815-38828.
4. Kim, T. H.,Yu, B.-S.,Ko, H. W.,Park, N. W.,Saeed, M. A.,Ahn, J.,Jo, S.,Kim, D.-Y.,Yoon, S. K.,Lee, K.-H.,Jeong, S. Y.,Woo, H. Y.,Kim, H. J.,Kim, T. G.,Park, J.,Park, M.-C.,Hwang, D. K.,Shim, J. W., *Adv. Mater.* **2024,** *36*, 2307523.
5. Wang, J.,Sun, L.,Xiong, S.,Du, B.,Yokota, T.,Fukuda, K.,Someya, T., *ACS Appl. Mater.*

Interfaces **2023,** *15*, 21314-21323.

6. Gao, Y.,Yu, Y.,Guo, J.,Sun, R.,Wang, T.,Wang, W.,Min, J., *Adv. Opt. Mater.* **2023,** *11*, 2202685.
7. Cutting, C. L.,Bag, M.,Venkataraman, D., *J. Mater. Chem. C* **2016,** *4*, 10367-10370.
8. Park, S.,Adhi Wibowo, F. T.,Krishna, N. V.,Ryu, J.,Lee, H.,Lee, J. H.,Yoon, Y. J.,Kim, J. Y.,Seo, J. H.,Oh, S.-H.,Jang, S.-Y.,Cho, S., *J. Mater. Chem. A* **2021,** *9*, 15394-15403.
9. Yang, Z.,Guan, C.,Jiang, X.,Zhang, G.,Xie, C.,Liu, C.,Xiao, C.,Li, W., *Sol. RRL* **2022,** *6*, 2100981.
10. Zhou, X.,Wu, H.,Bothra, U.,Chen, X.,Lu, G.,Zhao, H.,Zhao, C.,Luo, Q.,Lu, G.,Zhou, K.,Kabra, D.,Ma, Z.,Ma, W., *Mater. Horiz.* **2023,** *10*, 566-575.
11. Wang, W.,Cui, Y.,Zhang, T.,Bi, P.,Wang, J.,Yang, S.,Wang, J.,Zhang, S.,Hou, J., *Joule* **2023,** *7*, 1067-1079.
12. Lei, W.,Wang, Y.,Liang, Z.,Feng, J.,Zhang, W.,Fang, J.,Chen, Z.,Hou, L., *Adv. Energy Mater.* **2023,** *13*, 2301755.
13. Cui, Y.,Wang, Y.,Bergqvist, J.,Yao, H.,Xu, Y.,Gao, B.,Yang, C.,Zhang, S.,Inganäs, O.,Gao, F.,Hou, J., *Nat. Energy* **2019,** *4*, 768-775.
14. Cho, Y.,Kumari, T.,Jeong, S.,Lee, S. M.,Jeong, M.,Lee, B.,Oh, J.,Zhang, Y.,Huang, B.,Chen, L.,Yang, C., *Nano Energy* **2020,** *75*, 104896.
15. Park, S. Y.,Labanti, C.,Luke, J.,Chin, Y.-C.,Kim, J.-S., *Adv. Energy Mater.* **2022,** *12*, 2103237.
16. Bi, P.,Ren, J.,Zhang, S.,Wang, J.,Chen, Z.,Gao, M.,Cui, Y.,Zhang, T.,Qin, J.,Zheng, Z.,Ye, L.,Hao, X.,Hou, J., *Nano Energy* **2022,** *100*, 107463.
17. Luo, S.,Bai, F.,Zhang, J.,Zhao, H.,Angunawela, I.,Zou, X.,Li, X.,Luo, Z.,Feng, K.,Yu, H.,Wong, K. S.,Ade, H.,Ma, W.,Yan, H., *Nano Energy* **2022,** *98*, 107281.
18. Guan, S.,Li, Y.,Xu, C.,Yin, N.,Xu, C.,Wang, C.,Wang, M.,Xu, Y.,Chen, Q.,Wang, D.,Zuo, L.,Chen, H., *Adv. Mater.* **2024,** 2400342.
19. Song, J.,Zhang, C.,Li, C.,Qiao, J.,Yu, J.,Gao, J.,Wang, X.,Hao, X.,Tang, Z.,Lu, G.,Yang, R.,Yan, H.,Sun, Y., *Angew. Chem., Int. Ed.* **2024,** *63*, e202404297.
20. Yang, S.,Chen, Z.,Zhu, J.,Yang, D.,Wang, H.,Ding, P.,Wu, J.,Yan, P.,Xie, L.,Chen, F.,Wang, Y.,Zhang, J.,Ge, Z., *Adv. Mater.* **2024,** *36*, 2401789.

21. Kim, T. H.,Park, N. W.,Saeed, M. A.,Jeong, S. Y.,Woo, H. Y.,Park, J.,Shim, J. W., *Nano Energy* **2023,** *112*, 108429.
22. Yang, W.,Wang, W.,Wang, Y.,Sun, R.,Guo, J.,Li, H.,Shi, M.,Guo, J.,Wu, Y.,Wang, T.,Lu, G.,Brabec, C. J.,Li, Y.,Min, J., *Joule* **2021,** *5*, 1209-1230.
23. Bai, F.,Zhang, J.,Zeng, A.,Zhao, H.,Duan, K.,Yu, H.,Cheng, K.,Chai, G.,Chen, Y.,Liang, J.,Ma, W.,Yan, H., *Joule* **2021,** *5*, 1231-1245.
24. Lee, C.,Lee, J.-H.,Lee, H. H.,Nam, M.,Ko, D.-H., *Adv. Energy Mater.* **2022,** *12*, 2200275.
25. Xu, T.,Deng, B.,Zheng, K.,Li, H.,Wang, Z.,Zhong, Y.,Zhang, C.,Lévêque, G.,Grandidier, B.,Bachelot, R.,Treguer-Delapierre, M.,Qi, Y.,Wang, S., *Adv. Mater.* **2024,** *36*, 2311305.
26. Deng, B.,Shen, Y.,Zheng, K.,Wang, C.,Lévêque, G.,Xu, T., *Sol. RRL* **2023,** *7*, 2300211.
27. Xu, T.,Luo, Y.,Wu, S.,Deng, B.,Chen, S.,Zhong, Y.,Wang, S.,Lévêque, G.,Bachelot, R.,Zhu, F., *Adv. Sci.* **2022,** *9*, 2202150.
28. Mavridi-Printezi, A.,Menichetti, A.,Guernelli, M.,Montalti, M., *Nanoscale* **2021,** *13*, 9147-9159.
29. Huang, C.-L.,Kumar, G.,Sharma, G. D.,Chen, F.-C., *Appl. Phys. Lett.* **2020,** *116*, 253302.
30. Yuan, M.,Liu, S.,Li, H.,Gao, Y.,Yu, S.,Yu, Y.,Meng, L.,Liu, W.,Zhang, J.,Gao, P., *Adv. Compos. Hybrid Mater.* **2023,** *6*, 55.
31. Chen, Z.-H.,Yin, H.,Ho, J. K. W.,Cui, L.-Y.,So, S. K.,Hao, X.-T., *Appl. Phys. Lett.* **2021,** *118*, 043301.
32. Zhou, L.,Ou, Q.-D.,Chen, J.-D.,Shen, S.,Tang, J.-X.,Li, Y.-Q.,Lee, S.-T., *Scientific Reports* **2014,** *4*, 4040.
33. Ding, Y.,Young, M.,Zhao, Y.,Traverse, C.,Benard, A.,Lunt, R. R., *Solar Energy Materials and Solar Cells* **2015,** *132*, 523-527.
34. Leever, B. J.,Bailey, C. A.,Marks, T. J.,Hersam, M. C.,Durstock, M. F., *Adv. Energy Mater.* **2012,** *2*, 120-128.
35. Tan, J.,Zhao, Y.,Li, G.,Yang, S.,Huang, C.,Yu, H., *Adv. Funct. Mater.* **2022,** *32*, 2209094.
36. Liu, S.,Li, H.,Wu, X.,Chen, D.,Zhang, L.,Meng, X.,Tan, L.,Hu, X.,Chen, Y., *Adv. Mater.* **2022,** *34*, 2201604.
37. Koster, L. J. A.,Mihailetchi, V. D.,Ramaker, R.,Blom, P. W. M., *Appl. Phys. Lett.* **2005,**

86, 123509.

38. Koster, L. J. A.,Mihailetchi, V. D.,Blom, P. W. M., *Appl. Phys. Lett.* **2006,** *88*, 052104.
39. Kyaw, A. K. K.,Wang, D. H.,Gupta, V.,Leong, W. L.,Ke, L.,Bazan, G. C.,Heeger, A. J., *ACS Nano* **2013,** *7*, 4569-4577.
40. Lian, H.,Pan, M.,Han, J.,Cheng, X.,Liang, J.,Hua, W.,Qu, Y.,Wu, Y.,Dong, Q.,Wei, B.,Yan, H.,Wong, W.-Y., *J. Mater. Chem. A* **2021,** *9*, 16500-16509.
41. Anger, P.,Bharadwaj, P.,Novotny, L., *Phys. Rev. Lett.* **2006,** *96*, 113002.
42. Xu, T.,Deng, B.,Zhao, Y.,Wang, Z.,Lévêque, G.,Lambert, Y.,Grandidier, B.,Wang, S.,Zhu, F., *Adv. Energy Mater.* **2023,** *13*, 2301367.
43. Dudem, B.,Jung, J. W.,Yu, J. S., *J. Mater. Chem. A* **2018,** *6*, 14769-14779.
44. Dudem, B.,Heo, J. H.,Leem, J. W.,Yu, J. S.,Im, S. H., *J. Mater. Chem. A* **2016,** *4*, 7573-7579.
45. Lan, W.,Wang, Y.,Singh, J.,Zhu, F., *ACS Photonics* **2018,** *5*, 1144-1150.